

# Intraflagellar Transport Dynein is Autoinhibited by Trapping of its Mechanical and Track-Binding Elements

Katerina Toropova<sup>1</sup>, Miroslav Mladenov<sup>1</sup>, Anthony J. Roberts<sup>1\*</sup>

<sup>1</sup>Institute of Structural and Molecular Biology, Birkbeck, London, United Kingdom.

\*Correspondence should be addressed to A.J.R. (a.roberts@mail.cryst.bbk.ac.uk).

## ABSTRACT

Cilia are multi-functional organelles that are constructed using intraflagellar transport (IFT) of cargo to and from their tip. It is widely held that the retrograde IFT motor, dynein-2, must be controlled in order to reach the ciliary tip and then unleashed to power the return journey. However, the mechanism is unknown. Here, we systematically define the mechanochemistry of human dynein-2 motors as monomers, dimers, and multi-motor assemblies with kinesin-II. Combining these data with insights from single-particle electron microscopy, we discover that dynein-2 dimers are intrinsically autoinhibited. Inhibition is mediated by trapping dynein-2's mechanical "linker" and "stalk" domains within a novel motor-motor interface. We find that linker-mediated inhibition enables efficient transport of dynein-2 by kinesin-II *in vitro*. These results suggest a conserved mechanism for autoregulation among dimeric dyneins, which is exploited as a switch for dynein-2's recycling activity during IFT.

## Introduction

A major question in structural cell biology is how micrometer-scaled organelles are constructed and maintained. Cilia (also known as eukaryotic flagella) are multi-functional organelles that emanate from almost all cell types in the human body and many other eukaryotes <sup>1</sup>. Non-motile cilia serve as “signaling antennae” in processes as diverse as morphogenesis, mechanosensation, and olfaction <sup>2</sup>. Motile cilia beat with a wave-like motion essential for numerous propulsive functions <sup>3</sup>. Severe congenital disorders are caused by defects in cilia <sup>3</sup>, igniting interest in the mechanisms of ciliary assembly <sup>4</sup>.

The basis for the formation and maintenance of cilia is a conserved motor-protein-driven process, called intraflagellar transport (IFT) <sup>5</sup>. Cilia are supported by an axoneme of nine microtubule doublets (**Fig. 1a**). During assembly, cilia elongate from their distal tip <sup>6</sup>. IFT is a bidirectional transport system that moves ciliary components synthesized in the cytoplasm to the tip of the cilium, and returns products to the cell body. Cargoes of IFT include both structural (e.g. tubulin) and functional (e.g. G-protein coupled receptor) components <sup>1,2,7-9</sup>.

IFT is powered by ATP-fueled motors that move along the outer surface of the microtubule doublets. The principal motor driving anterograde movement to the ciliary tip is heterotrimeric kinesin-II (Kif3 in humans), augmented by a homodimeric kinesin-II in some cilia <sup>10</sup>. Kinesin-II motility is beginning to be understood in detail <sup>10-13</sup>. Universally, retrograde IFT is driven by dynein-2 <sup>14-18</sup> (also known as dynein 1b or IFT dynein), which is the subject of this study. Dynein-2 is a dimer of two ~0.5 MDa heavy chains, each of which possesses a motor domain, together with several associated chains <sup>19</sup> (**Fig. 1a**). Its closest relative is cytoplasmic dynein-1, the major motor driving transport to microtubule minus ends in the cytoplasm <sup>20</sup>. Despite rapid progress in dynein-1 research <sup>21,22</sup> and advances in defining dynein-2 composition <sup>23-25</sup>, the motility and regulation of dynein-2 in IFT are poorly understood.

Indeed, unlike cytoplasmic transport, for which detailed models are emerging for some cargo types, relatively little is known about the motor mechanisms involved in IFT. Notably, IFT differs from cytoplasmic transport in several striking ways. First, dynein-2 and kinesin-II are integrated into long (~220 nm) linear arrays termed “IFT trains” containing multiple copies of each motor <sup>26,27</sup>, in contrast to the small groups of membrane-bound motors typical of cytoplasmic transport <sup>28</sup>. Second, rather than stochastic back-and-forth switches in direction characteristic of cytoplasmic transport, the activity of

dynein-2 and kinesin-II is highly coordinated: IFT trains travel to the tip of the cilium (kinesin direction) then return to the base (dynein direction) in an apparently deterministic fashion<sup>28</sup>. Finally, rather than involving conventional regulators of cytoplasmic dynein-1 motility, such as dynactin, Nudel and Lis1<sup>22</sup>, the factors controlling dynein-2 motility are mysterious.

The nature of dynein-2 motility itself is also unclear, a situation compounded by the challenges of working with the large dynein-2 mechanoenzyme *in vitro*. Rapid retrograde IFT has been observed in living cells with velocities ranging from 140 – 7,400 nm/s<sup>29</sup>. However, *in vitro* assays with a partial dynein-2 complex yielded slow movement at ~70 nm/s<sup>30</sup>, raising the question of how fast movement is elicited *in vivo*.

Structural information is available for dynein-2's motor domain in monomeric form<sup>31</sup>, revealing a classic dynein subdomain organization (**Fig. 1a**). The catalytic core is a ring of six AAA+ modules, of which AAA1 is the main ATPase site. Microtubule binding occurs at the tip of an anti-parallel coiled coil "stalk". A C-terminal domain (CTD) lies on one face of the ring. Opposite lies dynein's mechanical element, the "linker" domain, which arches from AAA1 over the ring and connects to the dimerizing N-terminal tail. The linker undergoes a nucleotide-dependent power stroke<sup>32-34</sup>, involving a bent-to-straight transition, which is thought to transmit force between the two motor domains and to cargo<sup>31,35-37</sup>. It is widely held that dynein-2 force generation must be regulated in time and space, in order for the complex to move as a passenger to the ciliary tip before powering return transport in the opposite direction<sup>1</sup>. How dynein-2 mechanochemistry is regulated is unknown.

In this work, we systematically define the motile properties of human dynein-2 motor domains as monomers, dimers, and multi-motor assemblies with kinesin-II. Integrating these data with structural insights from electron microscopy (EM), we find that dynein-2 dimers are intrinsically autoinhibited. Rather than involving the CTD, previously implicated in dynein-1 autoregulation<sup>38</sup>, inhibition is mediated by trapping of dynein-2's mechanical linker and track-binding stalk within a novel motor-motor interface. Inhibited dynein-2 dimers are efficiently transported by kinesin-II *in vitro*, whereas disrupting linker-mediated interaction activates dynein-2 and retards anterograde transport. These findings suggest a conserved basis for autoregulation among dimeric dyneins, which is co-opted as a switch for dynein-2's recycling activity in IFT.

## RESULTS

### Mechanochemistry of the dynein-2 motor domain

A foundation for understanding the mechanisms of other cytoskeletal motors has been a robust source of purified protein. To dissect the action and regulation of dynein-2, we used insect cells to express a human monomeric dynein-2 motor domain (Dyn2<sub>motor</sub>) with a SNAP<sub>f</sub> tag at its amino terminus (**Fig. 1b**). The SNAP<sub>f</sub>-tag enabled covalent labeling of Dyn2<sub>motor</sub> with a variety of ligands (bright fluorophores, biotin or DNA oligonucleotides), which we used for single-molecule visualization, surface immobilization, and attaching the motor to DNA origami structures respectively. Dyn2<sub>motor</sub> was separated from excess ligand using size-exclusion chromatography (**Fig. 2a**), yielding purified (**Fig. 2b**) monomeric protein (**Fig. 2c**).

To determine the motile properties of Dyn2<sub>motor</sub>, we biotinylated it and attached it to a neutravidin-coated surface. Upon addition of microtubules and ATP, Dyn2<sub>motor</sub> powered fast gliding of microtubules as visualized by TIRF microscopy (**Fig. 2d** and **Supplementary Video 1**). Notably, the velocity of microtubule gliding varied depending on the surface density of Dyn2<sub>motor</sub>. Movement was rapid ( $524.0 \pm 7.5$  nm/s;  $\pm$  standard error of the fit, here and elsewhere unless specified) at high input concentrations of Dyn2<sub>motor</sub> ( $> 20$  nM), and decreased gradually as the surface density was lowered (**Fig. 2e**). This concentration relationship indicates that fast microtubule movement is a property of Dyn2<sub>motor</sub> ensembles. Indeed, at intermediate Dyn2<sub>motor</sub> concentrations, longer microtubules were translocated faster than short ones (**Supplementary Fig. 1a,b**), suggesting that the number of motors interacting per microtubule is the critical parameter influencing velocity.

Enzymatically, Dyn2<sub>motor</sub> hydrolyzed an average of  $1.3 \pm 0.1$  ATPs/second. This basal rate was stimulated by microtubules to yield a  $k_{cat}$  of  $4.8 \pm 0.9$  ATPs/second (**Fig. 2f**). The continuous and rapid microtubule motion driven by Dyn2<sub>motor</sub> (**Fig. 2d**) differs from the erratic and slow ( $\sim 70$  nm/s) motility reported for a partial dynein-2 complex purified from HEK cells<sup>30</sup>. The absolute velocity and concentration dependence of microtubule movement varied depending on buffer type and ionic strength (**Supplementary Fig. 1c**); a phenomenon that is likely to have contributed to the slower velocities reported earlier<sup>30,31</sup>. Together, these data reveal that the dynein-2 motor domain powers fast microtubule movement in monomer ensembles.

### Dimerization inhibits dynein-2 ATPase and motility

We next tested if motor domains within dynein-2 dimers influence one another's activity. Cytoplasmic dyneins have shown great plasticity as dimers, retaining motor function when the N-terminal tail is replaced with a variety of dimerizing moieties<sup>39-44</sup> (GST, coiled coils, FRB/FKBP, and DNA). We therefore dimerized Dyn2<sub>motor</sub> using GST (**Fig. 1b**), enabling comparison to well-studied GST cytoplasmic dynein-1 constructs. As expected, GST-Dyn2<sub>motor</sub> was a stable dimer (**Fig. 3c**).

Strikingly, dimerization inhibited, rather than stimulated, the motility and ATPase activity of Dyn2<sub>motor</sub>. The maximal rate of microtubule gliding was reduced to  $242.1 \pm 4.2$  nm/s, while the concentration dependence of movement remained similar (**Fig. 3d**). In ATPase assays, the basal rate of hydrolysis by GST-Dyn2<sub>motor</sub> was  $0.9 \pm 0.1$  ATPs/second. GST-Dyn2<sub>motor</sub> ATPase was only minimally activated by microtubules, saturating at a maximal rate of  $1.9 \pm 0.3$  ATPs/second (**Fig. 3e**). Thus, dimerization perturbs the response of Dyn2<sub>motor</sub> to its allosteric activator, the microtubule. Control experiments revealed that GST *per se* is not responsible for the repressed motility of GST-Dyn2<sub>motor</sub> (below). These results indicate that GST-Dyn2<sub>motor</sub> behavior arises from interactions between its two motor domains.

Imaging at the single-molecule level revealed that GST-Dyn2<sub>motor</sub> bound transiently to microtubules in the presence of ATP, typically dwelling for less than a second per encounter, without undergoing measurable movement (**Fig. 3f**). This behavior differs from the robust processivity of *S. cerevisiae* dynein-1 GST dimers<sup>39</sup>, being more akin to mammalian dynein-1<sup>38,42,45,46</sup>. In summary, we conclude that pairing two dynein-2 motor domains substantially inhibits their enzymatic and microtubule gliding activities.

### Dynein-2 dimers adopt a stacked conformation

To gain insight into how the two dynein-2 motor domains influence each other's activity, we examined the structure of GST-Dyn2<sub>motor</sub> using single-particle negative stain EM. In the presence of ATP, GST-Dyn2<sub>motor</sub> molecules displayed a distinctive "stacked" conformation (**Fig. 4a,b**), in which the AAA+ rings of the two motor domains are closely apposed (**Supplementary Fig. 2c**). This appearance recalls the compact "Phi-particle" shape observed for cytoplasmic dynein-1<sup>38,46,47</sup>, which is a putatively inhibited state<sup>38</sup> (**Supplementary Fig. 3d**). Protruding from dynein-2's AAA+ rings, the coiled-coil stalk and globular microtubule-binding domain at its tip are visible (**Fig. 4a**). Invariantly, the stalks cross each other at a fixed angle, intersecting at a distance one-third along their length

**(Supplementary Video 2).** Given the inherent flexibility of dynein's stalk, these observations indicate an interaction between the coiled coils at the crossing site.

Stacking of GST-Dyn2<sub>motor</sub> was nucleotide dependent. In the absence of nucleotide or in ADP conditions, the AAA+ rings were separated, exhibiting a wide range of motor-motor distances (**Fig. 4b, Supplementary Fig. 2a,c** and **Supplementary Video 2**), in contrast to the sharp distribution of low motor-motor distances characteristic of stacking in ATP. Stacking was also observed in the ADP.Vi (vanadate) state (mimicking the ADP.Pi state) (**Fig. 4b** and **Supplementary Fig. 2a,c**). The linker – the main mechanical element of dynein – is straight in no nucleotide and ADP states, but bent in the ATP and ADP.Vi states<sup>20</sup>, raising the possibility that stacking is promoted by a bent linker.

Stacking of GST-Dyn2<sub>motor</sub> in ATP was almost entirely abolished by the addition of 500 mM salt (**Fig. 4b** and **Supplementary Fig. 2a,c**), suggesting that the stacking interface has an electrostatic component and is comparatively weak. In line with a weak interaction, spontaneous stacking between Dyn2<sub>motor</sub> monomers was not observed at the nM concentrations of our EM experiments (**Fig. 2c**). However, after dimerization, which holds the Dyn2<sub>motor</sub> protomers at a high local concentration >0.2 mM (derived from their maximum separation of 30 nm in unstacked molecules), the large majority of molecules are stacked, with only a small subset showing large motor-motor separation (**Supplementary Fig. 2c**). These data indicate that 1) in ATP conditions, the majority of dynein-2 motor domains adopt a stacked conformation, and 2) stacking is metastable and could be influenced by external cues.

### **The linker and stalk are trapped at the stacking interface**

We next determined the spatial arrangement of the two dynein-2 motor domains in the stacked configuration, exploiting our EM data and the availability of a crystal structure of a monomeric dynein-2 motor construct<sup>31</sup>. Although dynein-2 has only been crystallized as a monomer, it is in the ADP.Vi state. As the linker domain is bent in this state, we predicted it to be capable of forming the stacking interface (**Fig. 4b**). Moreover, while monomeric dynein-2 motors do not stack spontaneously in solution, the high effective concentrations during crystallization might promote formation of the stacking interface, analogous to the high local concentration within GST-Dyn2<sub>motor</sub> dimers. We therefore searched the crystal lattice, and found pairs of dynein-2 monomers that quantitatively resemble the stacked molecules we observed in isolated GST-Dyn2<sub>motor</sub> dimers (**Fig. 4c, Supplementary Fig. 3c** and **Supplementary Video 3**).

The major interface between the paired dynein-2 motors involves the linker domains (**Fig. 4c**). It features a cluster of side chain contacts between the linkers at their distal tips, and an interaction between the fourth AAA+ module (AAA4) in the ring and the linker near its hinge. Additional inter-motor contacts occur between the AAA5 modules at their helix 2 and  $\beta$ -hairpin insert, and between the coiled-coil stalks as they cross, consistent with our EM analysis. All contacts are detailed in **Supplementary Fig. 3b**. The C-terminal domains are located opposite to the interface, and do not interact. This architecture contrasts with the existing model of autoinhibition in dynein-1<sup>38</sup>, which evoked an interaction between motors through their C-terminal domains (**Supplementary Fig. 3a**).

To test if linker-mediated interaction is responsible for the stacked dynein-2 conformation observed by EM, we mutated to alanine three charged or polar amino acids at the linker-AAA4 interface (**Fig. 5a**). Specifically, we targeted linker residues that are predicted to hydrogen bond with AAA4 (D1406/Q1407/R1410). The resulting construct [GST-Dyn2(DQR)<sub>motor</sub>] remained dimerized, but stacking was almost completely abolished (**Fig. 4b, 5c** and **Supplementary Fig. 2b**). The motors displayed a wide range of separations, with a distribution similar to the parental wild-type construct in no nucleotide or ADP (**Supplementary Fig. 2c**). Quantitative comparison shows that linker-mediated stacking not only matches the dynein-2 EM data (**Supplementary Fig. 3c**), but provides a similarly strong match to class averages of the dynein-1 holoenzyme Phi particle (**Supplementary Fig. 3d**). Thus, the stacked arrangement of dynein-2 motor domains in GST-Dyn2<sub>motor</sub> is strikingly similar to dynein-1 motor domains natively dimerized by the tail. These data indicate that the linker-mediated interaction may be ancient and conserved, predating the ancestor of dynein-1 and 2. We conclude that paired dynein-2 motors domains stack via an interface involving their main mechanical element – the linker domain.

### **Untrapping dynein-2's linker and stalk rescues ATPase and motility**

Inspection of dynein-2 motor stacking indicates incompatibility with dynein motility at three levels (**Fig. 4d**). First, the linker - dynein's mechanical amplifier - is not free to move, being trapped in the bent conformation at the interface between the motor domains. The linker's essential docking site at AAA5<sup>36</sup> is also directly occluded. Second, the two microtubule-binding domains point in opposite directions, meaning that they could not engage the microtubule simultaneously, as proposed<sup>38</sup>. Finally, consistent with our EM analysis, the coiled-coil stalks interact at their crossing point. This contact is

likely to restrict intra-coiled-coil helix sliding in the stalk, which canonically mediates communication between dynein's ATPase and microtubule-binding sites, and is essential for mechanochemistry<sup>48,49</sup>.

If linker-mediated stacking is the basis for inhibition in GST-Dyn2<sub>motor</sub> dimers, then disrupting the stacking interface should rescue motility. Restoration of activity in a GST dimer would also demonstrate that GST *per se* is not responsible for inhibition. We therefore determined the motile behavior of the unstacked GST-Dyn2(DQR)<sub>motor</sub> mutant. Importantly, the DQR substitution had little or no impact on dynein-2 motility and ATPase in the context of a monomer, showing that the mutations do not intrinsically affect motor activity (**Supplementary Fig. 4c,d**). However, in the context of a dimer, the unstacking DQR mutations had a significant impact. The maximum velocity of microtubule gliding increased to  $562.2 \pm 4.7$  nm/s (**Fig. 5e**), restoring it to the level of the Dyn2<sub>motor</sub> monomer (**Fig. 2e**), while the concentration dependence remained similar. The ATPase of GST-Dyn2(DQR)<sub>motor</sub> was elevated to a maximal rate  $4.1 \pm 0.2$  ATPs/second at saturating microtubule concentrations (**Fig. 5d**), again similar to Dyn2<sub>motor</sub>. As expected from the concentration dependence of microtubule gliding (**Fig. 5e**), measurably processive movement by GST-Dyn2(DQR)<sub>motor</sub> single molecules was extremely rare. However, the landing rate of GST-Dyn2(DQR)<sub>motor</sub> on the microtubule was elevated relative to GST-Dyn2<sub>motor</sub> (**Fig. 5f**), consistent with the availability of its microtubule-binding domains. Together, these findings indicate that linker-mediated stacking is responsible for the inhibition of dynein-2 dimers; furthermore, they suggest that rupture of linker stacking activates dynein-2 to a level comparable to the isolated motor domain.

### **Linker-mediated inhibition facilitates dynein-2 transport as a cargo of kinesin Kif3**

What is the role of linker-mediated stacking of dynein-2 in intraflagellar transport? One possibility is that it provides the basis for dynein-2 to be targeted to the tip of the cilium by kinesin-II in a switched-off state; a phenomenon that has been long suspected but never tested or rationalized<sup>1</sup>. To test this notion, we built a multi-motor assembly of dynein-2 and kinesin-II. Pioneering studies in *Chlamydomonas* indicate that IFT motors are linked together *in vivo* by linear arrays of ~22 different proteins (the IFT-A and IFT-B complexes)<sup>50-52</sup>. However, IFT trains tend to fall apart during purification from cilia<sup>50</sup> and vary in length<sup>26</sup> so motor composition is not preserved or controlled following isolation, while recombinantly expressed IFT sub-complexes have not formed arrays, even at high concentrations<sup>53</sup>. Thus, native protein-based methods have been unable to systematically assemble multiple IFT motors *in vitro*.

To obtain control over the composition of dynein-2 and kinesin-II per assembly, we used a synthetic-biology inspired approach, and coupled them via a programmable DNA origami chassis<sup>54</sup> (**Fig. 6a**). For kinesin-II, we developed a Kif3 construct with a C-terminal SNAP<sub>f</sub> tag, yielding an active motor that can be labeled with single-stranded (ss) DNA (**Supplementary Fig. 5**). For the chassis, we used a 12-helix DNA bundle design, in which a specified number of ss sequences project from one of its helices<sup>54</sup>. These “handle” sequences serve as specific attachment sites for DNA-labeled Kif3 or dynein-2. Use of three attachment sites per motor facilitates comparison with similar cytoplasmic motor assemblies<sup>54</sup>. As visualized by EM, the dimensions of the DNA structure (225 nm x 14 nm) approximate an IFT train<sup>27</sup> (**Fig. 6b**). We refer to these IFT motor-DNA assemblies herein as synthetic “trains”.

In the absence of dynein-2, trains bearing human Kif3 motors bound to and traveled along microtubules towards the plus end with a mean velocity of ~600 nm/s (**Fig. 6c**), similar to Kif3 from other species<sup>10</sup>, slightly slower than single human Kif3 motors (**Supplementary Fig. 5f**), and within the range of anterograde IFT velocities reported in vertebrate cilia<sup>29</sup>. Notably, upon addition of GST-Dyn2<sub>motor</sub>, train movement remained uniformly plus-end-directed (**Fig. 6c**). Trains exhibited a range of speeds, with peak velocities similar to trains bearing Kif3 alone, and a tail of slower velocities (**Fig. 6d**). The latter may reflect stochastic unstacking and activation of GST-Dyn2<sub>motor</sub> (**Fig. 4b**, top right panel). The uniform train movement towards the plus end distinguishes IFT motor assemblies from those with *S. cerevisiae* dynein-1 and human kinesin-1, in which most events were minus-end directed or stalled in a tug-of-war<sup>54</sup>. These results indicate that GST-Dyn2<sub>motor</sub> provides little resistance to Kif3, resulting in transit of both motors to the plus end of the microtubule. To determine if linker-mediated inhibition facilitates GST-Dyn2<sub>motor</sub> transport as a cargo of Kif3, we replaced it with GST-Dyn2(DQR)<sub>motor</sub> – the mutant deficient in linker-mediated inhibition. In comparison to GST-Dyn2<sub>motor</sub>, GST-Dyn2(DQR)<sub>motor</sub> severely retarded train motility. Movement remained plus-end directed, but most trains were brought to a virtual standstill with velocities <150 nm/s (**Fig. 6c,d**). Thus, we conclude that linker-mediated inhibition prevents dynein-2 motors from conferring strong resistance to Kif3, enabling efficient transit of both motors to the plus end of the microtubule.

Finally, we asked if teams of dynein-2 motors could power processive minus-end-directed movement when coupled on a train. The precise number of motors per IFT train *in vivo* is uncertain, with fluorescence and force-based estimates ranging between 4 and 40<sup>13,55,56</sup>. We found that, *in vitro*,

synthetic trains with 3 attachment sites for GST-Dyn2<sub>motor</sub> or GST-Dyn2(DQR)<sub>motor</sub> exhibited processive movements infrequently (not shown), as did assemblies with 7 GST-Dyn2<sub>motor</sub> (**Supplementary Fig. 6b**). In contrast, trains with 7 GST-Dyn2(DQR)<sub>motor</sub> sites displayed robust processive movement towards microtubule minus ends, with an average and maximal velocity of  $334.0 \pm 4.7$  ( $\pm$  SEM) and 572.1 nm/s respectively (**Fig. 6e**). The mean travel distance was  $3.5 \pm 0.2$  microns ( $\pm$  SEM). These results suggest that when teams of dynein-2 motors are activated by untrapping their linkers and stalks, they power continuous movement over distances comparable to the length of a primary cilium.

## DISCUSSION

Using purified human proteins, mechanochemical assays, EM, and synthetic-biology-inspired engineering, we have obtained insights into dynein-2 activity significant for understanding the molecular mechanism of IFT. First, monomeric dynein-2 motor domains are capable of driving fast microtubule gliding *in vitro*, approaching the velocities of retrograde IFT in vertebrate cells<sup>29</sup>. Second, the motility and ATPase of dynein-2 motor domains are inhibited upon dimerization (their natural oligomeric status). Third, within dimers, dynein-2 motor domains tend to associate via a novel interface that traps their linker domains and crosses their microtubule-binding stalks, shutting down their activities. Fourth, mutations that disrupt this entrapment activate dynein-2 dimers, restoring their ATPase and motility while causing them to strongly resist kinesin-II.

We integrate these data and previous studies into a model for dynein-2 regulation, which enables efficient cycles of IFT (**Fig. 7**). We propose that following its synthesis and dimerization in the cytosol, dynein-2 intrinsically adopts the inhibited configuration. In this switched-off state, with its linkers trapped and stalks crossed, dynein-2 is loaded onto anterograde IFT trains near the base of the cilium. It is transported as a passenger to the ciliary tip by kinesin-II. At the tip of the cilium, a localized signal activates dynein-2. A key feature is disrupting the inhibitory interface we define, unshackling dynein-2's mechanical and track-binding elements. This enables them to power the return transport of turnover products, IFT machinery, and signaling molecules out of the cilium<sup>2</sup>, completing the IFT cycle. This model applies to the force-generating heavy chains of dynein-2. Its associated subunits may be labile, associating and dissociating from the complex, giving rise to distinct dynamics<sup>57</sup>. In essence, dynein-2 is naturally in an off state.

One role of linker-mediated inhibition in dynein-2 may be to limit futile ATP hydrolysis, akin to other cytoskeletal motors<sup>58</sup>. However, we find that the ATPase of dynein-2's motor domain is

comparatively low. Thus, we suggest that a major function of linker-mediated inhibition in IFT is to prevent interference and a tug-of-war between dynein-2 and kinesin-II<sup>59</sup>, which would impair anterograde delivery of cargoes and clog the confined space between the axoneme and ciliary membrane.

Point mutations in dynein-2 are associated with Jeune asphyxiating thoracic dystrophy and short rib polydactyly, typically lethal congenital disorders characterized by shortened ribs<sup>19</sup>. Morphologically, loss of dynein-2 function is associated with stumpy cilia with accumulations of IFT particles at their tip<sup>16,17</sup>. If mutations that constitutively activate dynein-2 still permit anterograde IFT train attachment, they may have even more severe impact *in vivo*, by disrupting anterograde IFT and kinesin-II, both of which are vital for ciliogenesis.

The mechanism of dynein-2 autoinhibition identified by this work may be tuned by cellular factors. We interpret our EM data and the residual gliding and microtubule-stimulated ATPase activities of GST-Dyn2<sub>motor</sub> to reflect an equilibrium between inhibited and active forms<sup>38</sup>. This balance could be tuned by anterograde IFT train attachment, the dynein-2 tail, or its associated subunits. It was recently discovered that within *Chlamydomonas* cilia, anterograde IFT occurs on the B-tubule of the doublet, whereas retrograde transport is on the A-tubule<sup>27</sup>. The tubulin subunits within each tubule are enriched with distinct post-translational modifications<sup>60</sup>, and those on the B-tubule could tune dynein-2's microtubule interactions during anterograde IFT.

Our finding that association between dynein-2 motor domains traps their linker domains, occludes the linker docking site on AAA5, and crosses their stalks provides a mechanistic basis for inhibition. It differs from the existing model for cytoplasmic dynein-1 autoregulation, which holds that motor domains associate into a Phi particle via their C-terminal domains<sup>38</sup>, leaving their linkers free to move on the periphery of the dimer. While it is possible that dynein-2 uses a different autoinhibitory interface to dynein-1, we favor that the linker-mediated mechanism is conserved in both dynein classes. First, we find that the chemistry of key amino acids in the linker-mediated interface is conserved between dynein-2 and dynein-1 (**Fig. 5b**). A notable exception is found in *S. cerevisiae* dynein-1, which is a constitutively active motor. Second, the linker-mediated interaction explains the observed nucleotide dependency of the Phi-particle architecture<sup>38</sup>, as it is only sterically possible when the linker is bent. Finally, the atomic model of dynein-2 in the inhibited form provides a compelling match to images of the cytoplasmic dynein-1 Phi particle. Thus, linker-mediated inhibition serves as a model for all

autoregulated dynein dimers. At ångström resolution, since the stacking model derives from ADP.Vi dynein-2 *in crystallo*, minor differences might be expected compared with dynein-2 in solution; crucially, however, our structure-guided mutagenesis shows that the linker-mediated interaction is fundamental to stacking and autoinhibition.

Our results sharpen focus on the mechanisms of dynein-2 activation and IFT train turnaround at the ciliary tip, which have been visualized at the fluorescence-microscopy level *in situ*<sup>2</sup>. They suggest that a key step in dynein-2 activation is rupture of the linker-mediated interface we define (“untrapping”). In addition, IFT train turnaround at the ciliary tip requires kinesin-II deactivation and/or detachment<sup>1</sup>. Kinesin-II deactivation may be achieved by an intramolecular interaction between its tail and motor domains<sup>58,61,62</sup>. Detachment of kinesin-II from the IFT train, while not occurring in all cilia, is reported to arise from direct phosphorylation of one of the kinesin heavy chains in *Chlamydomonas*<sup>63</sup>. In a related manner, dynein-2 could be activated by direct post-translational modification of its inhibitory interface, for example phosphorylation by a tip-localized kinase. Indeed, serine and threonine residues lie at the interface (**Supplementary Fig. 3b**), although they are not highly conserved. Our favored alternative is a “train-centric” model for dynein-2 activation. Here, the reported “remodeling” of the IFT train at the ciliary tip<sup>64</sup> would create a distinct binding site for dynein-2 that forces apart and re-orient its motor domains, analogous to dynactin binding to cytoplasmic dynein-1<sup>65,66</sup>. A difference between the motor-centric and train-centric IFT models is that in the former, each dynein-2 complex would need to reach the ciliary tip in order to receive the activating signal, whereas in the latter only the train would have to reach the tip, whereas individual dyneins could exchange between trains, being locally activated on those that have been remodeled. Single-molecule imaging of dynein-2 heavy chains within cilia could help to distinguish between these models. These activating steps would occur downstream of the major conceptual event arising from this work: namely, dynein-2 being carried to the ciliary tip by kinesin-II in an inhibited state, with its mechanical elements trapped and stalks crossed (**Fig. 7**). For cytoplasmic dynein, a conserved inhibitory architecture is likely to control the motor’s many functions in vesicle trafficking, virus transport, mRNA localization, and chromosome segregation, which can be investigated using the interface residues established here.

## ACKNOWLEDGEMENTS

We thank C. Moores, G. Zanetti and A. Osborne for critical comments on the manuscript; M. Williams, S. Reck-Peterson and members of the Birkbeck EM group for advice; S. Nofal, S. Miah, and L.

Stejskal for initial experiments; and A. Carter (MRC-LMB, Cambridge) for plasmid DNA. This work was supported by a Sir Henry Dale Fellowship to A.J.R. from the Wellcome Trust and Royal Society [104196/Z/14/Z].

## AUTHOR CONTRIBUTIONS

K.T. and A.J.R. conducted biochemical and TIRF experiments. K.T. performed electron microscopy experiments. M.M. generated and purified constructs. K.T. and A.J.R. analyzed data and wrote the paper.

## COMPETING FINANCIAL INTERESTS STATEMENT

The authors declare no competing financial interests.

## REFERENCES:

1. Rosenbaum, J.L. & Witman, G.B. Intraflagellar transport. *Nat Rev Mol Cell Biol* **3**, 813-25 (2002).
2. Lehtreck, K.F. IFT-Cargo Interactions and Protein Transport in Cilia. *Trends Biochem Sci* **40**, 765-78 (2015).
3. Fliegauf, M., Benzing, T. & Omran, H. When cilia go bad: cilia defects and ciliopathies. *Nat Rev Mol Cell Biol* **8**, 880-93 (2007).
4. Ishikawa, H. & Marshall, W.F. Ciliogenesis: building the cell's antenna. *Nat Rev Mol Cell Biol* **12**, 222-34 (2011).
5. Kozminski, K.G., Johnson, K.A., Forscher, P. & Rosenbaum, J.L. A motility in the eukaryotic flagellum unrelated to flagellar beating. *Proc Natl Acad Sci U S A* **90**, 5519-23 (1993).
6. Johnson, K.A. & Rosenbaum, J.L. Polarity of flagellar assembly in *Chlamydomonas*. *J Cell Biol* **119**, 1605-11 (1992).
7. Hao, L. et al. Intraflagellar transport delivers tubulin isotypes to sensory cilium middle and distal segments. *Nat Cell Biol* **13**, 790-8 (2011).
8. Bhogaraju, S. et al. Molecular basis of tubulin transport within the cilium by IFT74 and IFT81. *Science* **341**, 1009-12 (2013).
9. Kubo, T. et al. Together, the IFT81 and IFT74 N-termini form the main module for intraflagellar transport of tubulin. *J Cell Sci* **129**, 2106-19 (2016).
10. Scholey, J.M. Kinesin-2: a family of heterotrimeric and homodimeric motors with diverse intracellular transport functions. *Annu Rev Cell Dev Biol* **29**, 443-69 (2013).
11. Andreasson, J.O., Shastry, S., Hancock, W.O. & Block, S.M. The Mechanochemical Cycle of Mammalian Kinesin-2 KIF3A/B under Load. *Curr Biol* **25**, 1166-75 (2015).
12. Albracht, C.D., Guzik-Lendrum, S., Rayment, I. & Gilbert, S.P. Heterodimerization of Kinesin-2 KIF3AB Modulates Entry into the Processive Run. *J Biol Chem* **291**, 23248-56 (2016).
13. Prevo, B., Mangeol, P., Oswald, F., Scholey, J.M. & Peterman, E.J. Functional differentiation of cooperating kinesin-2 motors orchestrates cargo import and transport in *C. elegans* cilia. *Nat Cell Biol* **17**, 1536-45 (2015).
14. Gibbons, B.H., Asai, D.J., Tang, W.J., Hays, T.S. & Gibbons, I.R. Phylogeny and expression of axonemal and cytoplasmic dynein genes in sea urchins. *Mol Biol Cell* **5**, 57-70 (1994).
15. Pazour, G.J., Wilkerson, C.G. & Witman, G.B. A dynein light chain is essential for the retrograde particle movement of intraflagellar transport (IFT). *J Cell Biol* **141**, 979-92 (1998).
16. Pazour, G.J., Dickert, B.L. & Witman, G.B. The DHC1b (DHC2) isoform of cytoplasmic dynein is required for flagellar assembly. *J Cell Biol* **144**, 473-81 (1999).
17. Porter, M.E., Bower, R., Knott, J.A., Byrd, P. & Dentler, W. Cytoplasmic dynein heavy chain 1b is required for flagellar assembly in *Chlamydomonas*. *Mol Biol Cell* **10**, 693-712 (1999).

18. Signor, D. et al. Role of a class DHC1b dynein in retrograde transport of IFT motors and IFT raft particles along cilia, but not dendrites, in chemosensory neurons of living *Caenorhabditis elegans*. *J Cell Biol* **147**, 519-30 (1999).
19. Hou, Y. & Witman, G.B. Dynein and intraflagellar transport. *Exp Cell Res* **334**, 26-34 (2015).
20. Roberts, A.J., Kon, T., Knight, P.J., Sutoh, K. & Burgess, S.A. Functions and mechanics of dynein motor proteins. *Nat Rev Mol Cell Biol* **14**, 713-26 (2013).
21. Carter, A.P., Diamant, A.G. & Urnavicius, L. How dynein and dynactin transport cargos: a structural perspective. *Curr Opin Struct Biol* **37**, 62-70 (2016).
22. Cianfrocco, M.A., DeSantis, M.E., Leschziner, A.E. & Reck-Peterson, S.L. Mechanism and regulation of cytoplasmic dynein. *Annu Rev Cell Dev Biol* **31**, 83-108 (2015).
23. Patel-King, R.S., Gilberti, R.M., Hom, E.F. & King, S.M. WD60/FAP163 is a dynein intermediate chain required for retrograde intraflagellar transport in cilia. *Mol Biol Cell* **24**, 2668-77 (2013).
24. Asante, D., Stevenson, N.L. & Stephens, D.J. Subunit composition of the human cytoplasmic dynein-2 complex. *J Cell Sci* **127**, 4774-87 (2014).
25. Schmidts, M. et al. TCTEX1D2 mutations underlie Jeune asphyxiating thoracic dystrophy with impaired retrograde intraflagellar transport. *Nat Commun* **6**, 7074 (2015).
26. Mencarelli, C., Mitchell, A., Leoncini, R., Rosenbaum, J. & Lupetti, P. Isolation of intraflagellar transport trains. *Cytoskeleton* **70**, 439-52 (2013).
27. Stepanek, L. & Pigino, G. Microtubule doublets are double-track railways for intraflagellar transport trains. *Science* **352**, 721-4 (2016).
28. Hancock, W.O. Bidirectional cargo transport: moving beyond tug of war. *Nat Rev Mol Cell Biol* **15**, 615-28 (2014).
29. Williams, C.L. et al. Direct evidence for BBSome-associated intraflagellar transport reveals distinct properties of native mammalian cilia. *Nat Commun* **5**, 5813 (2014).
30. Ichikawa, M., Watanabe, Y., Murayama, T. & Toyoshima, Y.Y. Recombinant human cytoplasmic dynein heavy chain 1 and 2: observation of dynein-2 motor activity in vitro. *FEBS Lett* **585**, 2419-23 (2011).
31. Schmidt, H., Zalyte, R., Urnavicius, L. & Carter, A.P. Structure of human cytoplasmic dynein-2 primed for its power stroke. *Nature* **518**, 435-8 (2015).
32. Burgess, S.A., Walker, M.L., Sakakibara, H., Knight, P.J. & Oiwa, K. Dynein structure and power stroke. *Nature* **421**, 715-8 (2003).
33. Kon, T., Mogami, T., Ohkura, R., Nishiura, M. & Sutoh, K. ATP hydrolysis cycle-dependent tail motions in cytoplasmic dynein. *Nat Struct Mol Biol* **12**, 513-9 (2005).
34. Roberts, A.J. et al. AAA+ Ring and linker swing mechanism in the dynein motor. *Cell* **136**, 485-95 (2009).
35. Kon, T. et al. The 2.8 Å crystal structure of the dynein motor domain. *Nature* **484**, 345-50 (2012).
36. Schmidt, H., Gleave, E.S. & Carter, A.P. Insights into dynein motor domain function from a 3.3-Å crystal structure. *Nat Struct Mol Biol* **19**, 492-7 (2012).
37. Roberts, A.J. et al. ATP-driven remodeling of the linker domain in the dynein motor. *Structure* **20**, 1670-80 (2012).
38. Torisawa, T. et al. Autoinhibition and cooperative activation mechanisms of cytoplasmic dynein. *Nat Cell Biol* **16**, 1118-24 (2014).
39. Reck-Peterson, S.L. et al. Single-molecule analysis of dynein processivity and stepping behavior. *Cell* **126**, 335-48 (2006).
40. Shima, T., Imamula, K., Kon, T., Ohkura, R. & Sutoh, K. Head-head coordination is required for the processive motion of cytoplasmic dynein, an AAA+ molecular motor. *J Struct Biol* **156**, 182-9 (2006).
41. Qiu, W. et al. Dynein achieves processive motion using both stochastic and coordinated stepping. *Nat Struct Mol Biol* **19**, 193-200 (2012).
42. Trokter, M., Mucke, N. & Surrey, T. Reconstitution of the human cytoplasmic dynein complex. *Proc Natl Acad Sci U S A* **109**, 20895-900 (2012).
43. Imai, H. et al. Direct observation shows superposition and large scale flexibility within cytoplasmic dynein motors moving along microtubules. *Nat Commun* **6**, 8179 (2015).
44. Nicholas, M.P. et al. Control of cytoplasmic dynein force production and processivity by its C-terminal domain. *Nat Commun* **6**, 6206 (2015).
45. McKenney, R.J., Huynh, W., Tanenbaum, M.E., Bhabha, G. & Vale, R.D. Activation of cytoplasmic dynein motility by dynactin-cargo adapter complexes. *Science* **345**, 337-41 (2014).

46. Schlager, M.A., Hoang, H.T., Urnavicius, L., Bullock, S.L. & Carter, A.P. In vitro reconstitution of a highly processive recombinant human dynein complex. *EMBO J* **33**, 1855-68 (2014).
47. Amos, L.A. Brain dynein crossbridges microtubules into bundles. *J Cell Sci* **93 ( Pt 1)**, 19-28 (1989).
48. Gibbons, I.R. et al. The affinity of the dynein microtubule-binding domain is modulated by the conformation of its coiled-coil stalk. *J Biol Chem* **280**, 23960-5 (2005).
49. Kon, T. et al. Helix sliding in the stalk coiled coil of dynein couples ATPase and microtubule binding. *Nat Struct Mol Biol* **16**, 325-33 (2009).
50. Cole, D.G. et al. Chlamydomonas kinesin-II-dependent intraflagellar transport (IFT): IFT particles contain proteins required for ciliary assembly in *Caenorhabditis elegans* sensory neurons. *J Cell Biol* **141**, 993-1008 (1998).
51. Piperno, G. & Mead, K. Transport of a novel complex in the cytoplasmic matrix of *Chlamydomonas* flagella. *Proc Natl Acad Sci U S A* **94**, 4457-62 (1997).
52. Taschner, M. & Lorentzen, E. The Intraflagellar Transport Machinery. *Cold Spring Harb Perspect Biol* **8**, a028092 (2016).
53. Taschner, M. et al. Intraflagellar transport proteins 172, 80, 57, 54, 38, and 20 form a stable tubulin-binding IFT-B2 complex. *EMBO J* **35**, 773-90 (2016).
54. Derr, N.D. et al. Tug-of-war in motor protein ensembles revealed with a programmable DNA origami scaffold. *Science* **338**, 662-5 (2012).
55. Engel, B.D., Ludington, W.B. & Marshall, W.F. Intraflagellar transport particle size scales inversely with flagellar length: revisiting the balance-point length control model. *J Cell Biol* **187**, 81-9 (2009).
56. Shih, S.M. et al. Intraflagellar transport drives flagellar surface motility. *Elife* **2**, e00744 (2013).
57. Li, W., Yi, P. & Ou, G. Somatic CRISPR-Cas9-induced mutations reveal roles of embryonically essential dynein chains in *Caenorhabditis elegans* cilia. *J Cell Biol* **208**, 683-92 (2015).
58. Verhey, K.J. & Hammond, J.W. Traffic control: regulation of kinesin motors. *Nat Rev Mol Cell Biol* **10**, 765-77 (2009).
59. Belyy, V. et al. The mammalian dynein-dynactin complex is a strong opponent to kinesin in a tug-of-war competition. *Nat Cell Biol* **18**, 1018-24 (2016).
60. Yu, I., Garnham, C.P. & Roll-Mecak, A. Writing and Reading the Tubulin Code. *J Biol Chem* **290**, 17163-72 (2015).
61. Brunnbauer, M. et al. Regulation of a heterodimeric kinesin-2 through an unprocessive motor domain that is turned processive by its partner. *Proc Natl Acad Sci U S A* **107**, 10460-5 (2010).
62. Imanishi, M., Endres, N.F., Gennerich, A. & Vale, R.D. Autoinhibition regulates the motility of the *C. elegans* intraflagellar transport motor OSM-3. *J Cell Biol* **174**, 931-7 (2006).
63. Liang, Y. et al. FLA8/KIF3B phosphorylation regulates kinesin-II interaction with IFT-B to control IFT entry and turnaround. *Dev Cell* **30**, 585-97 (2014).
64. Pedersen, L.B., Geimer, S. & Rosenbaum, J.L. Dissecting the molecular mechanisms of intraflagellar transport in *Chlamydomonas*. *Curr Biol* **16**, 450-9 (2006).
65. Urnavicius, L. et al. The structure of the dynactin complex and its interaction with dynein. *Science* **347**, 1441-6 (2015).
66. Chowdhury, S., Ketcham, S.A., Schroer, T.A. & Lander, G.C. Structural organization of the dynein-dynactin complex bound to microtubules. *Nat Struct Mol Biol* **22**, 345-7 (2015).

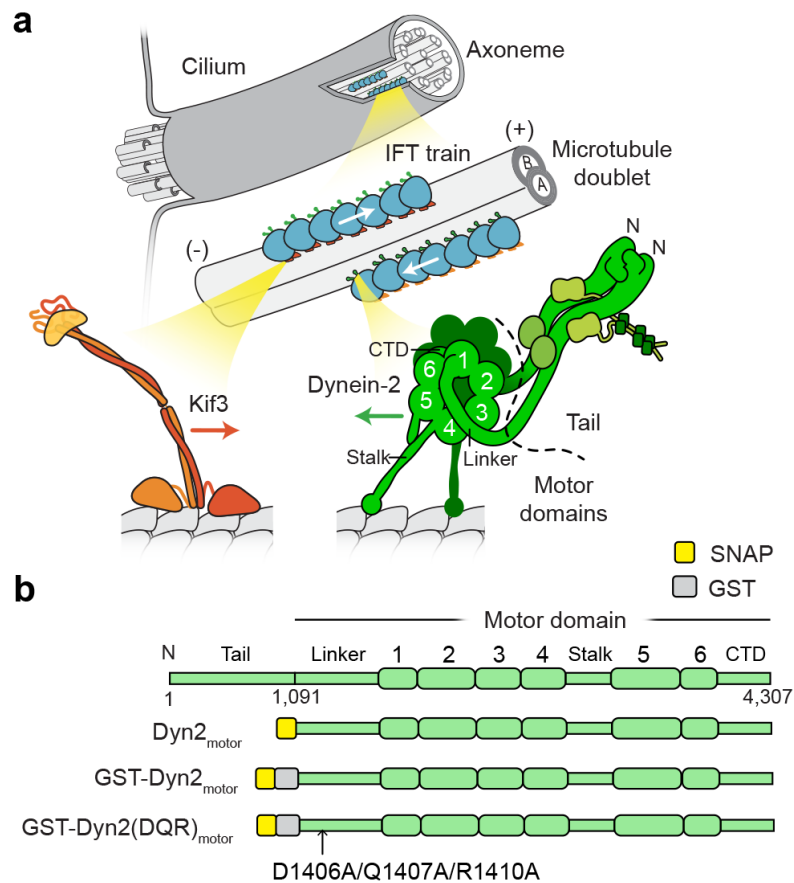


**Figure 1 – Intraflagellar transport motors and constructs used in this study.**

(a) Series of enlargements depicting the cilium; its constituent microtubule doublets; IFT trains that move cargoes along the microtubule doublets; and the motors that power train movement. (+) and (-) indicate microtubule polarity. Kinesin-II family member Kif3 powers transport towards the ciliary tip. Dynein-2 powers transport towards the cell body, functioning as a homodimer of two heavy chains and several associated subunits. Each heavy chain contains a motor domain including the linker, six AAA+ modules (1-6), C-terminal domain (CTD), and microtubule-binding stalk.

(b) Linear diagrams of the dynein-2 heavy chain and key motor domain constructs used in this study.

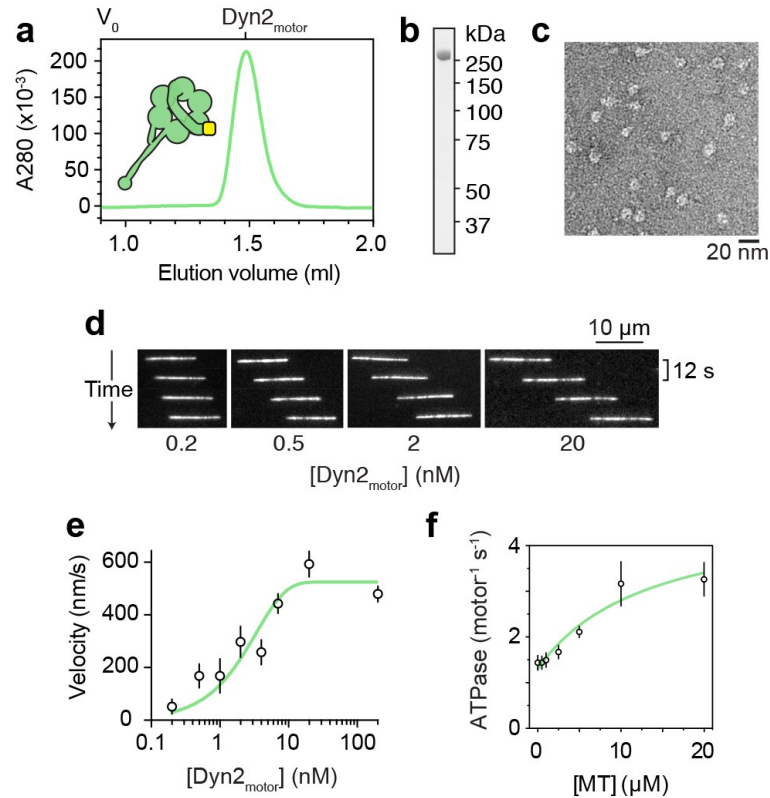


**Figure 2 – Monomeric dynein-2 motor domains power fast microtubule gliding.**

(a) Size-exclusion chromatogram of Dyn2<sub>motor</sub> and schematic of the construct.  $V_0$ ; void volume.

(b) SDS-PAGE of Dyn2<sub>motor</sub> after the final purification step.

(c) Negative stain EM of Dyn2<sub>motor</sub> monomers in ATP.

(d) Time sequence of microtubule translocation by surface immobilized Dyn2<sub>motor</sub> at different input concentrations. See also **Supplementary Video 1**.

(e) Plot of mean microtubule gliding velocity ( $\pm$  SD) at different Dyn2<sub>motor</sub> concentrations. Fitted values ( $\pm$  standard error of the fit):  $V_{\max} = 524.0 \pm 7.5$  nm/s,  $f = 0.3 \pm 0.01$ . Number of microtubules analyzed per concentration: 0.2 nM (38), 0.5 nM (44), 1 nM (39), 2 nM (47), 4 nM (49), 7 nM (46), 20 nM (56), 200 nM (53).

(f) Microtubule stimulated ATPase activity of Dyn2<sub>motor</sub>. Experiments were carried out in triplicate, mean values ( $\pm$  SD) are shown. Fitted values ( $\pm$  standard error of the fit):  $k_{\text{cat}} = 4.8 \pm 0.9$  s<sup>-1</sup>,  $k_{\text{basal}} = 1.3 \pm 0.1$  s<sup>-1</sup>,  $K_m(\text{MT}) = 13.5 \pm 7.5$  μM. Source data for e-f are available online.

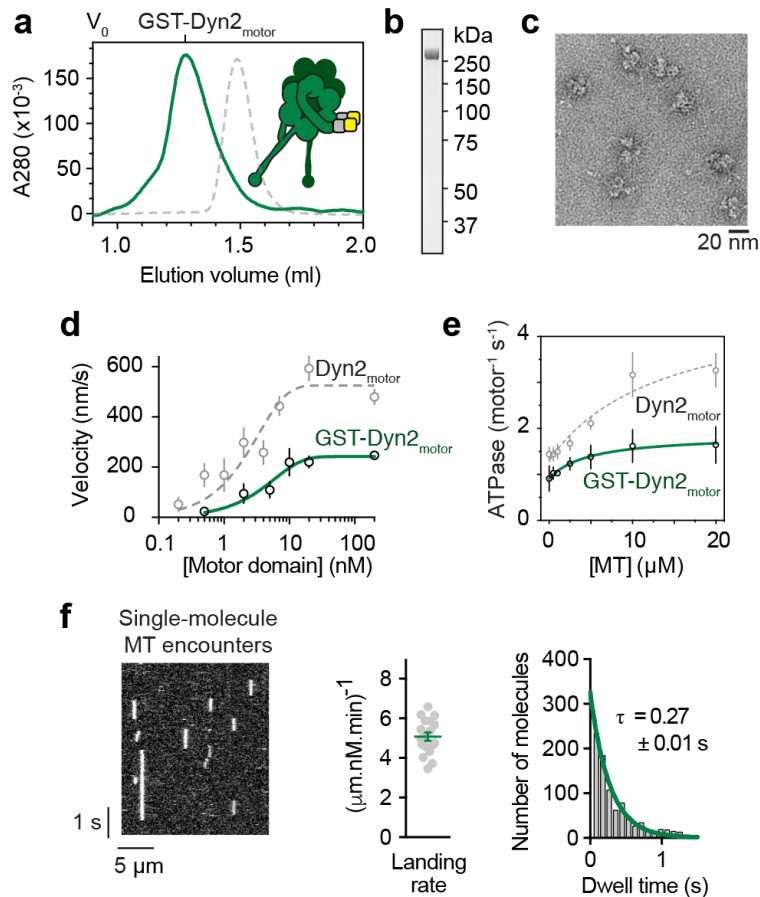


**Figure 3 – Dimerization inhibits dynein-2 motor domains.**

(a) Size-exclusion chromatogram of GST-Dyn2<sub>motor</sub> and schematic of the construct. For comparison, a normalized monomeric Dyn2<sub>motor</sub> trace is shown (dashed grey line). V<sub>0</sub>; void volume.

(b) SDS-PAGE of GST-Dyn2<sub>motor</sub> after the final purification step.

(c) Negative stain EM of GST-Dyn2<sub>motor</sub> dimers in ATP.

(d) Plot of mean microtubule gliding velocity ( $\pm$  SD) at different GST-Dyn2<sub>motor</sub> concentrations (Dyn2<sub>motor</sub> values from **Fig. 2e** are plotted in grey for comparison). Fitted values ( $\pm$  standard error of the fit):  $V_{\max} = 242.1 \pm 4.2$  nm/s,  $f = 0.2 \pm 0.01$ . Number of microtubules analyzed per concentration: 0.5 nM (33), 2 nM (24), 5 nM (38), 10 nM (45), 20 nM (48), 200 nM (48).

(e) Microtubule stimulated ATPase activity of GST-Dyn2<sub>motor</sub> (Dyn2<sub>motor</sub> values from **Fig. 2f** plotted in grey for comparison). Experiments were carried out in triplicate, mean values ( $\pm$  SD) are shown. Fitted values ( $\pm$  standard error of the fit):  $k_{\text{cat}} = 1.9 \pm 0.3$  s<sup>-1</sup>,  $k_{\text{basal}} = 0.9 \pm 0.1$  s<sup>-1</sup>,  $K_m(\text{MT}) = 4.8 \pm 4.2$   $\mu\text{M}$ .

(f) Single-molecule behavior of GST-Dyn2<sub>motor</sub>. (Left) Kymograph showing encounters of TMR-labeled GST-Dyn2<sub>motor</sub> with the microtubule in 1 mM ATP. (Middle) Quantification of microtubule landing rate. Green line; mean ( $\pm$  SEM). Number of landing rates: 18, from a total of 941 landing events over 18 microtubules. (Right) Histogram of GST-Dyn2<sub>motor</sub> dwell times on the microtubule, and single exponential decay fit (green). Number of dwell times: 927. Tau; average dwell time (decay constant<sup>-1</sup>)  $\pm$  standard error of the fit. Source data for **d-f** are available online.

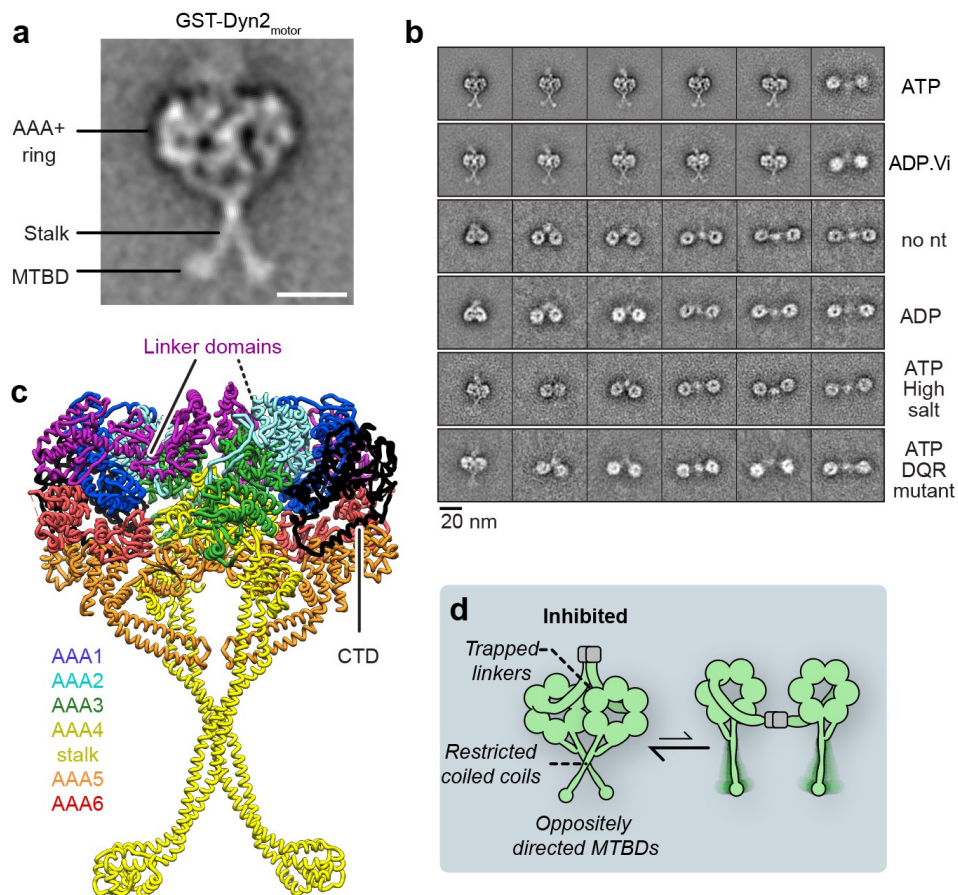


**Figure 4 – Dynein-2’s linker and stalk are trapped within a novel motor-motor interface.**

(a) EM class average of GST-Dyn2<sub>motor</sub> in 1 mM ATP. Subdomains are labeled. Scale bar; 10 nm. The AAA+ rings are closely apposed and stalks are crossed. MTBD; microtubule-binding domain.

(b) Example class averages of GST-Dyn2<sub>motor</sub> and GST-Dyn2(DQR)<sub>motor</sub> in different nucleotide and salt conditions. Nucleotide concentration; 1 mM. High salt; 500 mM KCl. GST-Dyn2<sub>motor</sub> molecules are predominantly stacked in ATP and ADP.Vi, while separated in other conditions. Stalks are not resolved in separated class averages owing to flexibility. Mutation of three amino acids within the linker (D1406A/Q1407A/R1410A; DQR mutant) almost abolishes stacking. See also **Supplementary Fig. 2**.

(c) Atomic model for the stacked arrangement of dynein-2 dimers in ATP and ADP.Vi conditions, derived from monomer crystal structure PDB 4RH7<sup>31</sup> as depicted in **Supplementary Video 3**. Linker domains and C-terminal domain (CTD) are indicated. AAA+ modules and stalk are colored according to the code.

(d) Schematic illustrating proposed structural mechanism of inhibition in stacked dynein-2 dimers (left), in equilibrium with the separated form (right).

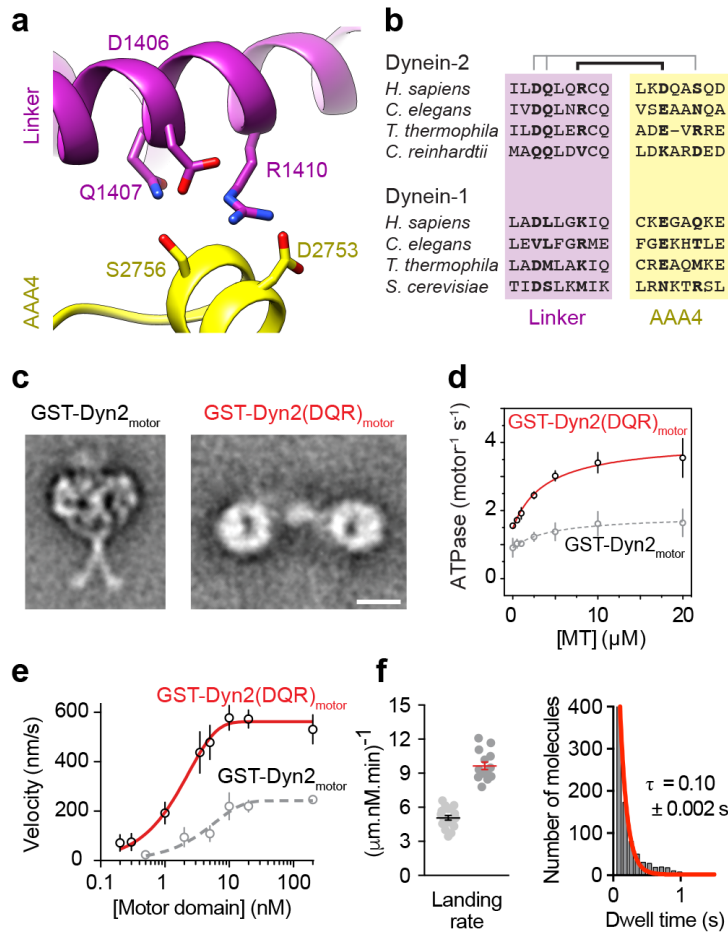


**Figure 5 – Untrapping dynein-2 dimers rescues their motility.**

(a) Depiction of amino acids within the linker and AAA4 module of dynein-2 predicted to form intermolecular hydrogen bonds crucial for stacking based upon the model of **Fig. 4c**.

(b) Amino acid conservation of residues shown in (a) among cytoplasmic dynein-1 and dynein-2 sequences. Pairs of interacting residues are indicated.

(c) Class averages of GST-Dyn2<sub>motor</sub> and GST-Dyn2(DQR)<sub>motor</sub> in ATP conditions. Scale bar; 10 nm.

(d) Microtubule-stimulated ATPase activity of GST-Dyn2(DQR)<sub>motor</sub> (GST-Dyn2<sub>motor</sub> values from **Fig. 3e** plotted in grey for comparison). Experiments were carried out in triplicate, mean values  $\pm$  SD are shown. Fitted values ( $\pm$  standard error of the fit):  $k_{cat} = 4.1 \pm 0.2$  s<sup>-1</sup>,  $k_{basal} = 1.5 \pm 0.1$  s<sup>-1</sup>,  $K_m(MT) = 3.9 \pm 1.2$  μM.

(e) Plot of mean microtubule gliding velocity ( $\pm$  SD) at different GST-Dyn2(DQR)<sub>motor</sub> concentrations (GST-Dyn2<sub>motor</sub> values from **Fig. 3d** plotted in grey for comparison). Fitted values ( $\pm$  standard error of the fit):  $V_{max} = 562.2 \pm 4.7$  nm/s,  $f = 0.4 \pm 0.01$ . Number of microtubules analyzed per concentration: 0.2 nM (29), 0.3 nM (34), 1 nM (31), 3.5 nM (20), 5 nM (34), 10 nM (53), 20 nM (46), 200 nM (42).

(f) (Left) Quantification of microtubule landing rate for GST-Dyn2(DQR)<sub>motor</sub>. Red line; mean  $\pm$  SEM.

Number of landing rates: 14, from a total of 956 landing events over 14 microtubules. Data for GST-Dyn2<sub>motor</sub> from **Fig. 3f** are shown alongside for comparison (black line). (Right) Histogram of GST-Dyn2(DQR)<sub>motor</sub> dwell times on the microtubule, and single-exponential decay fit (red).

Number of dwell times: 945. Tau; average dwell time (decay constant<sup>-1</sup>)  $\pm$  standard error of the fit. Source data for **d-f** are available online.

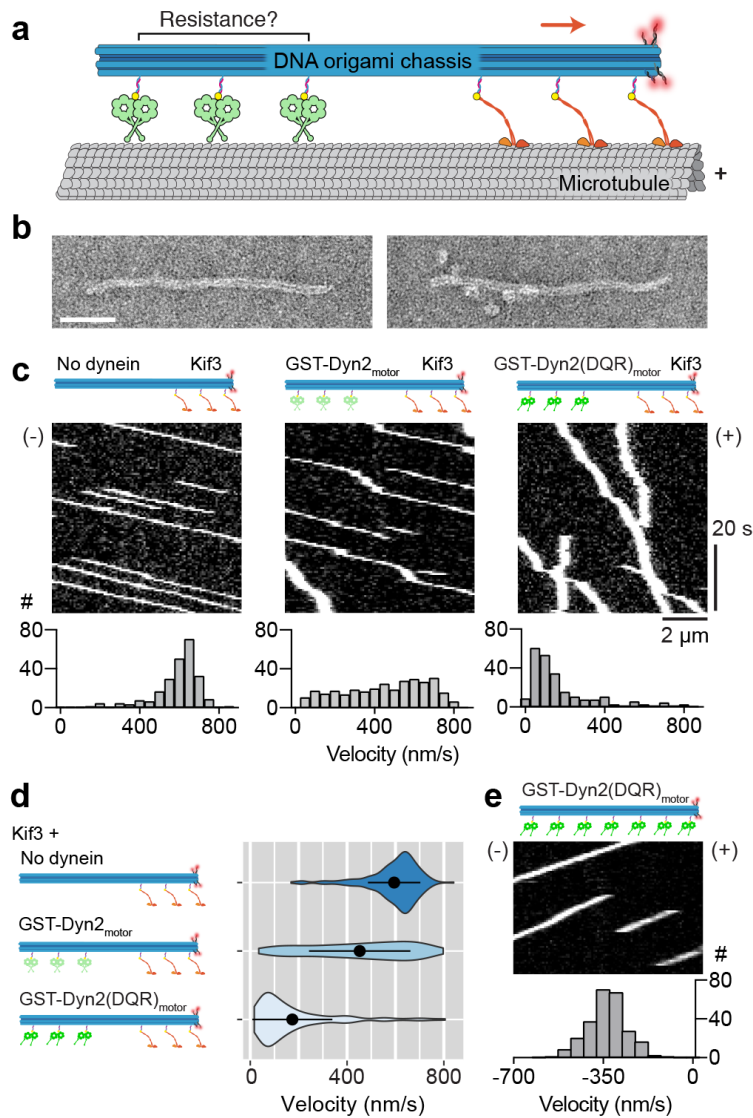


**Figure 6 – Assembly and motility of dynein-2 and kinesin Kif3 in multi-motor arrays.**

(a) Diagram of the experimental set-up. A DNA origami chassis physically links arrays of IFT motors (in this example 3 Kif3 and 3 dynein-2). The movement of the resulting assembly on the microtubule is visualized via tetramethylrhodamine-labeled DNAs (red spheres).

(b) Negative stain EM images of DNA origami chassis samples with 3 dynein-2 sites before (left) and after (right) incubation with GST-Dyn2<sub>motor</sub>. Scale bar; 50 nm.

(c) Kymographs of chassis with indicated types of motor. (+) and (-) indicate microtubule polarity. Velocity histograms are shown below, in which the Y axis represents number of events (#). Number of runs analyzed: Kif3 chassis (231), GST-Dyn2<sub>motor</sub>-Kif3 chassis (299), GST-Dyn2(DQR)<sub>motor</sub>-Kif3 chassis (222).

(d) Velocity distributions for chassis type depicted as violin plots, with mean ± SD shown. Mean ± SEM values: Kif3 chassis (594.6 ± 7.1 nm/s), GST-Dyn2<sub>motor</sub>-Kif3 chassis (452.3 ± 12.1 nm/s), GST-Dyn2(DQR)<sub>motor</sub>-Kif3 chassis (173.8 ± 11.1 nm/s).

(e) Kymograph of chassis with 7 GST-Dyn2(DQR)<sub>motor</sub> sites and velocity histogram below (N = 249). Negative velocity indicates movement toward the microtubule minus end. See also **Supplementary Fig. 6**. Source data for c-e are available online.

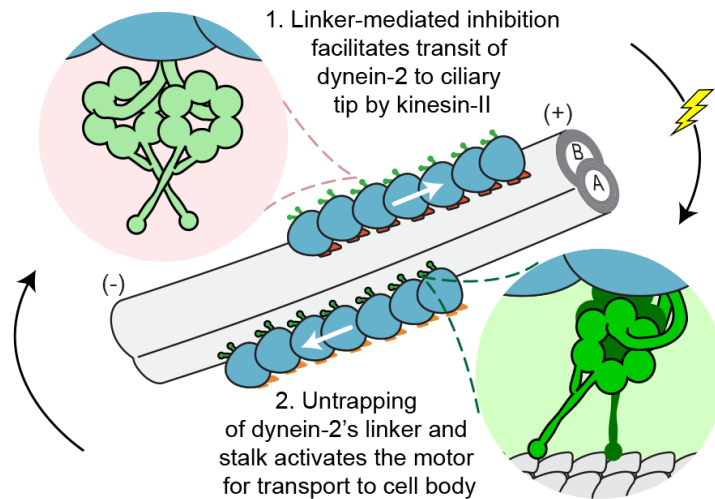


**Figure 7 – Model for dynein-2 regulation during IFT.**

Dynein-2 is carried in an autoinhibited state, with its linkers trapped and stalks crossed, towards the tip of the cilium on an IFT train (blue), together with cargoes essential for ciliary growth, maintenance and function (not depicted). The IFT train is propelled by kinesin-II (orange) along the microtubule doublet. At the ciliary tip, cargoes are unloaded, the IFT train is remodeled, and kinesin-II is inhibited (or detached). Dynein-2 is activated (lightning symbol) by untrapping of its linker and stalk, unleashing the activity of its motor domains to power return transport of the IFT train, along with cargoes destined for the cell body. See main text and references therein. (+) and (-) indicate microtubule polarity. A- and B-tubules of the microtubule doublet are indicated.

## ONLINE METHODS

**Protein expression.** Dynein-2, cytoplasmic dynein-1 and Kif3 constructs were expressed in *Spodoptera frugiperda* (Sf9) insect cells (Gibco) using the baculovirus system. A *H. sapiens* cytoplasmic dynein-2 construct codon-optimized for expression in Sf9 cells (Addgene #64064) was modified to replace the N-terminal GFP tag<sup>31</sup> with a GST tag and/or SNAP<sub>f</sub> tag. Components were amplified using Q5 polymerase (NEB) and gel purified before Gibson assembly. The resulting constructs encode dynein-2 (amino acids 1,091 – 4,307) with an N-terminal ZZ tag, TEV cleavage cassette, SNAP<sub>f</sub> tag, GST tag (as indicated), and an intervening glycine-serine spacer, within the pFastBac vector. The human cytoplasmic dynein-1 holoenzyme construct was as described<sup>46</sup>. Genes encoding *H. sapiens* Kif3A and Kif3B were synthesized (Epoch) with codon-optimization for Sf9 expression and substitutions that prevent autoinhibition (G485E/G486E and G477E/G478E, respectively) after Brunnbauer et al.<sup>61</sup>. Kif3A was inserted into the pACEBac1 vector (Geneva Biotech) with a C-terminal SNAP<sub>f</sub> tag and intervening glycine-serine spacer. Kif3B was inserted into the pACEBac1 vector with an N-terminal ZZ tag and TEV cleavage cassette. To prevent aggregation, putatively disordered regions at the C-termini of Kif3A (amino acids P600 - Q702) and Kif3B (P592 – K747) were removed.

Vectors containing constructs of interest flanked by Tn7 transposition sites were transformed into DH10EMBacY cells by heat shock or electroporation followed by selection on antibiotic plates. Colonies in which constructs had successfully transposed into the Tn7 site of the EMBacY bacmid were identified by blue/white screening. Bacmids were purified from 3 ml bacterial cultures by alkaline lysis and isopropanol precipitation, as described<sup>46</sup>.

Sf9 cells were cultured in Insect-XPRESS Medium + L-glutamine (Lonza) at 27 °C. Cultures were maintained at  $1 - 2 \times 10^6$  cells/ml in flasks with shaking at 100 rpm unless indicated. To prepare baculoviruses for protein expression, Sf9 cells were transfected with bacmids in 6-well plates. In a total volume of 100  $\mu$ l, 2  $\mu$ g bacmid DNA was mixed with medium and 3  $\mu$ l FuGene HD transfection reagent (Promega), incubated for 15 min, then added drop-wise to  $1 \times 10^6$  adherently growing Sf9 cells in 2 ml of medium. After 3-days incubation, the efficiency of transfection was evaluated by monitoring YFP expression from EMBacY using a Countess II FL cell counter equipped with an EVOS light cube for fluorescent imaging (Thermo Fisher Scientific). The supernatant (V<sub>0</sub> virus) was added to a 50 ml Sf9 culture and incubated for 3 days. The resulting supernatant (V<sub>1</sub> virus) was stored at 4 °C,

and used to infect 250-500 ml cultures at a ratio of 1% (v/v) for protein production. For Kif3 expression, cultures were co-infected with Kif3A and Kif3B viruses. Cell pellets were harvested by centrifugation, washed in 1x PBS solution, then flash frozen in liquid nitrogen and stored at -80 °C.

**Protein purification.** Protein purifications were performed at 4 °C. Frozen cell pellets from 250 ml Sf9 cultures were resuspended in 20 ml purification buffer (30 mM HEPES [pH 7.4], 300 mM KCl, 50 mM K-acetate, 2 mM Mg-acetate, 1 mM EGTA, 10% [v/v] glycerol, 1 mM DTT, 0.2 mM Mg-ATP, 1 mM PMSF) supplemented with a cOmplete™ EDTA-free Protease Inhibitor Cocktail (Roche). Cells were lysed using a Dounce homogenizer and 10 strokes with a small clearance pestle. Lysates were clarified by ultracentrifugation in a Type 70 Ti rotor at 183,960 g for 30 min. The supernatant was incubated for 1 hour on a roller with 1 ml IgG Sepharose 6 resin (GE Healthcare) pre-washed in purification buffer. Resin and bound-proteins were collected by gentle centrifugation at 670 g for 5 min, transferred into a 20 ml column, and washed with 2x 20 ml volumes of purification buffer and 1x 20 ml volume of TEV buffer (50 mM Tris [pH 7.5], 150 mM K-acetate, 2 mM Mg-acetate, 1 mM EGTA, 10% [v/v] glycerol, 1 mM DTT, 0.2 mM Mg-ATP). Proteins of interest were eluted by resuspending the resin in TEV buffer, adding 100 µg TEV protease, and incubating the reaction overnight on a roller. TEV-cleaved proteins were separated from the resin using an empty column, concentrated to 0.5 – 4 mg/ml using Amicon Ultra centrifugal filter devices (100 kDa cutoff), and cleared by ultracentrifugation in a TLA 110 rotor at 337,932 g for 6 min.

**Protein labeling.** SNAP<sub>F</sub>-tagged motor proteins (~2.5 µM) were labeled in 100 µl reactions with 10 – 20 µM SNAP ligand (SNAP-Cell TMR-Star, SNAP-Surface Alexa Fluor 647 [NEB], or SNAP-conjugated oligonucleotide). Reactions were incubated at 4 °C for 2 hours. Proteins were purified from excess SNAP ligand by size-exclusion chromatography on a Superose 6 Increase 3.2/300 column using an ÄKTAmicro system (GE Healthcare), pre-equilibrated with gel filtration buffer (50 mM Tris [pH 7.5], 150 mM K-acetate, 2 mM Mg-acetate, 1 mM EGTA, 5% [v/v] glycerol, 1 mM DTT, 0.1 mM Mg-ATP). Fractions (100 µl) were analyzed by SDS-PAGE on 4-12% Tris-Bis gels with Sypro Red staining (Thermo Fisher Scientific), and imaged using an FLA-3000 fluorescent image analyzer (Fujifilm). Peak fractions were flash frozen under liquid nitrogen in single-use aliquots and stored at -80 °C.

**DNA origami.** DNA origami chassis structures consisting of a 12-helix bundle with the specified number of motor protein attachment sites were folded and purified as described<sup>54,67</sup>, with the following modifications. Oligonucleotides were purchased in 96-well format from Eurofins Genomics. Folding reactions comprised 50 nM p8064 scaffold DNA (Tilbit Nanosystems), 250 nM staple oligos, 500 nM motor attachment oligos, and 2.5  $\mu$ M TMR oligo in folding buffer (5 mM Tris [pH 8.0], 1 mM EDTA, 16 mM MgCl<sub>2</sub>). After assembly on ice, reactions were transferred to a thermocycler pre-heated to 65 °C. The temperature was decreased from 65 °C to 61 °C in steps of 1 °C per hour, then from 60 °C to 40 °C in steps of 1 °C per two hours. Folded chassis was purified from excess oligos and misfolded species by ultracentrifugation through a 15 – 45% glycerol gradient in 0.5x TBE buffer supplemented with 11 mM MgCl<sub>2</sub>. Ultracentrifugation was performed at 191,986 g for 2 hours 10 min using a SW 55 rotor. Fractions containing folded structures were identified by electrophoresis using a 2% (w/v) agarose/0.5x TBE gel supplemented with 11 mM MgCl<sub>2</sub> and SYBR Safe stain. Peak chassis-containing fractions were incubated with oligo-labeled motors for 30 min on ice (5 nM chassis, 70 nM motors), and examined immediately by TIRF microscopy. Motor attachment was verified by gel shift<sup>54,67</sup> using a 0.7 % agarose/0.5x TBE gel supplemented with 11 mM MgCl<sub>2</sub> and 0.1% LDS.

**Microtubules.** Tubulin was purified and labeled with Alexa-488 or biotin as described<sup>68,69</sup>. To prepare taxol-stabilized microtubules, a mixture comprising 100  $\mu$ M tubulin, 1 mM GTP, 1 mM MgCl<sub>2</sub>, 1 mM DTT and 10% DMSO was assembled in BRB80 (80 mM PIPES [pH 6.9], 2 mM MgCl<sub>2</sub>, 1 mM EGTA) on ice, then incubated at 37 °C for 30 min. Following addition of an equal volume of BRB80 + 40  $\mu$ M taxol, the solution was incubated for a further 10 min at 37 °C, then stored at ambient temperature. For fluorescent visualization or surface attachment, 10% of Alexa-488 tubulin or biotin tubulin were included in the polymerization mixture respectively. Microtubules for ATPase assays were separated from unpolymerised tubulin by ultracentrifugation through a 60% glycerol cushion in BRB80 + 20  $\mu$ M taxol at 267,008 g for 30 min. Microtubule concentrations are expressed for the tubulin dimer.

**ATPase assays.** ATPase assays were performed using an EnzChek phosphate assay kit (Molecular Probes) as described<sup>70,71</sup>. The final reaction comprised: 50 nM dynein-2, 0 – 20  $\mu$ M taxol stabilized microtubules, 2 mM Mg-ATP, 200  $\mu$ M 2-amino-6-mercapto-7-methyl-purine riboside, 1 U/ml purine nucleoside phosphorylase, and BRB80 buffer supplemented with 1 mM DTT and 20  $\mu$ M taxol. A

SpectraMax Plus 384 microplate reader (Molecular Devices) was used to monitor the coupled reaction at 360 nm at 5 s intervals for 10 min. ATPase data were fit to the following equation<sup>70</sup>:  $k_{\text{obs}} = (k_{\text{cat}} - k_{\text{basal}}) \times [\text{MT}] / (K_{\text{m}}(\text{MT}) + [\text{MT}]) + k_{\text{basal}}$ .

**TIRF microscopy.** Fluorescently-labeled molecules were visualized on an Eclipse Ti-E inverted microscope with a CFI Apo TIRF 1.49 N.A. oil objective, Perfect Focus System, H-TIRF module, LU-N4 laser unit (Nikon) and a quad band filter set (Chroma). Images were recorded with 30 – 100 ms exposures on an iXon DU888 Ultra EMCCD camera (Andor), controlled with NIS-Elements AR Software (Nikon).

Motility assays were assembled in flow chambers made between glass slides, biotin-PEG coverslips, and double-sided tape. For microtubule gliding assays, chambers were sequentially incubated with 1) blocking solution (0.75% Pluronic F-127, 5 mg/ml casein) for >5 min, followed by two washes with B80-TK (80 mM PIPES [pH 6.9], 2 mM MgCl<sub>2</sub>, 1 mM EGTA, 1 mM DTT, 20 μM taxol, 50 mM KCl); 2) 0.5 mg/ml neutravidin for 2 min, followed by two washes with B80-TK; 3) biotinylated motor protein (0.2 – 200 nM) for 2 min, followed by two washes with B80-TK supplemented with 1 mg/ml casein; 4) 0.1 μM Alexa-488 microtubules in assay solution (B80-TK supplemented with 1 mg/ml casein, 1 mM Mg-ATP, 71 mM β-mercaptoethanol, 20 mM glucose, 300 μg/ml glucose oxidase, 60 μg/ml catalase).

Single-molecule assays were prepared similarly for steps 1-2, except washes were performed with B80-T buffer (80 mM PIPES [pH 6.9], 2 mM MgCl<sub>2</sub>, 1 mM EGTA, 1 mM DTT, 20 μM taxol). Then, chambers were incubated with: 3) 0.25 μM Alexa-488, biotinylated microtubules for 2 min, followed by two washes with B80-T supplemented with 1 mg/ml casein; 4) 0.1 – 10 nM of TMR-labeled motor protein in assay solution (B80-T with supplements as above). DNA origami experiments were performed in the same way, except a modified buffer (50 mM Tris [pH 8.0], 2 mM MgCl<sub>2</sub>, 1 mM EGTA, 1 mM DTT, 20 μM taxol, 100 mM KCl) was used to minimize non-specific interactions between DNA and the PEG coverslip, and the final assay solution contained 30 – 100 pM chassis-motor complex and Kif3-Alexa647 as a marker of microtubule polarity. Velocities and durations of microtubule association were calculated from kymographs generated in FIJI<sup>72</sup>. For dwell time analysis, microtubule associations ≥ 90 ms (3 frames) were analyzed. Dwell time data were fit with a single exponential decay. For microtubule gliding experiments, microtubules <25 μm were analyzed. Gliding

data were fit to the following equation:  $V_{\text{obs}}/V_{\text{max}} = 1 - (1 - f)^C$  where  $V_{\text{obs}}$  and  $V_{\text{max}}$  are the observed and maximal velocity of the microtubule respectively,  $C$  is the motor concentration and  $f$  expresses the dependence of  $V_{\text{obs}}$  on motor concentration<sup>73</sup>. Graphing, curve fitting and statistical analysis were performed in Prism5 (GraphPad) and R with the ggplot2<sup>74</sup> package.

**Electron microscopy.** Dynein samples were diluted to 50 – 75 nM in EM buffer (50 mM Tris [pH 7.5], 150 mM K-acetate, 2 mM Mg-acetate, 1 mM EGTA, 1 mM DTT, ± 500 mM KCl) and supplemented with appropriate nucleotide to 1 mM concentration. DNA origami was diluted to 7.5 – 10 nM in EM buffer or mixed with a 6-fold molar excess of oligonucleotide labeled dynein-2 for 30 min and diluted 10-fold in EM buffer. Samples were prepared for electron microscopy by either adding 4  $\mu\text{l}$  of specimen directly onto a glow-discharged continuous carbon grid (Electron Microscopy Sciences) or by pipetting ~4  $\mu\text{l}$  of 2% uranyl acetate, a small air gap and then ~4  $\mu\text{l}$  of sample into a single tip and depositing the contents onto the EM grid. Grids were then stained in three sequential drops of 75  $\mu\text{l}$  2% uranyl acetate, blotted and air dried. For DNA origami, grids were washed in three 75  $\mu\text{l}$  drops of EM buffer following sample application to remove glycerol prior to staining.

Micrographs were acquired using a Tecnai T12 microscope (FEI) operating at 120 kV with a tungsten electron source and a 4k x 4k CCD camera (Gatan US4000). The nominal magnification was 52,000X for DNA-origami or 67,000X for dynein specimens, giving a sampling of 2.09 and 1.64  $\text{\AA}/\text{pixel}$  at the object level respectively. Images were collected with a dose of 20 – 30  $\text{e}/\text{\AA}^2$  and a nominal defocus of -1  $\mu\text{m}$ . For dynein images, single particles were picked from the micrographs manually in RELION<sup>75</sup> and CTF corrected by phase flipping using CTFFIND3<sup>76</sup> and RELION. Particles were binned by 2 for subsequent processing, windowed into 200 x 200 pixel boxes, band-pass filtered (10  $\text{\AA}$  – 450  $\text{\AA}$ ) and centered in Imagic<sup>77</sup>.

For measurement of the motor-motor separation, images of dynein dimers were subjected to several rounds of classification and multi-reference alignment in Imagic resulting in classes containing an average of 10 images. The distance between centroid positions of the two motor domains in each class average was measured using Boxer<sup>78</sup>.

For computational comparison between EM class averages of dynein and the dynein-2 crystal structure model (PDB ID: 4RH7<sup>31</sup>) all steps were carried out in SPIDER<sup>79</sup>. The crystal structure was low-pass filtered to 30 – 40  $\text{\AA}$ . The resulting maps were then projected with an angular sampling of

5.5° and a -1 µm defocus CTF applied. The projections were aligned to each class average and scored by cross correlation to identify the best matching projection. Crystal structures were displayed using The PyMOL Molecular Graphics System (Version 1.7 Schrödinger, LLC) and UCSF Chimera software<sup>80</sup>.

**Data availability.** Source data underlying the graphical representations used in **Fig. 2e,f**; **Fig. 3d-f**; **Fig. 5d-f**; and **Fig.6c-e** are available with the paper online. Other relevant data are available from the corresponding author upon reasonable request. Coordinates for the linker-stacking model, derived from PDB 4RH7<sup>31</sup>, are available as Supplementary Data Set 1.

67. Goodman, B.S. & Reck-Peterson, S.L. Engineering defined motor ensembles with DNA origami. *Methods Enzymol* **540**, 169-88 (2014).
68. Castoldi, M. & Popov, A.V. Purification of brain tubulin through two cycles of polymerization-depolymerization in a high-molarity buffer. *Protein Expr Purif* **32**, 83-8 (2003).
69. Hyman, A. et al. Preparation of modified tubulins. *Methods Enzymol* **196**, 478-85 (1991).
70. Kon, T., Nishiura, M., Ohkura, R., Toyoshima, Y.Y. & Sutoh, K. Distinct functions of nucleotide-binding/hydrolysis sites in the four AAA modules of cytoplasmic dynein. *Biochemistry* **43**, 11266-74 (2004).
71. Cho, C., Reck-Peterson, S.L. & Vale, R.D. Regulatory ATPase sites of cytoplasmic dynein affect processivity and force generation. *J Biol Chem* **283**, 25839-45 (2008).
72. Schindelin, J. et al. Fiji: an open-source platform for biological-image analysis. *Nat Methods* **9**, 676-82 (2012).
73. Uyeda, T.Q., Kron, S.J. & Spudich, J.A. Myosin step size. Estimation from slow sliding movement of actin over low densities of heavy meromyosin. *J Mol Biol* **214**, 699-710 (1990).
74. Wickham, H. *ggplot2: Elegant graphics for data analysis*, (Springer Science & Business Media, 2009).
75. Scheres, S.H. RELION: implementation of a Bayesian approach to cryo-EM structure determination. *J Struct Biol* **180**, 519-30 (2012).
76. Mindell, J.A. & Grigorieff, N. Accurate determination of local defocus and specimen tilt in electron microscopy. *J Struct Biol* **142**, 334-47 (2003).
77. van Heel, M., Harauz, G., Orlova, E.V., Schmidt, R. & Schatz, M. A new generation of the IMAGIC image processing system. *J Struct Biol* **116**, 17-24 (1996).
78. Ludtke, S.J., Baldwin, P.R. & Chiu, W. EMAN: semiautomated software for high-resolution single-particle reconstructions. *J Struct Biol* **128**, 82-97 (1999).
79. Frank, J. et al. SPIDER and WEB: processing and visualization of images in 3D electron microscopy and related fields. *J Struct Biol* **116**, 190-9 (1996).
80. Pettersen, E.F. et al. UCSF Chimera--a visualization system for exploratory research and analysis. *J Comput Chem* **25**, 1605-12 (2004).